The structure of bow shocks formed by the interaction of pulsed-power driven magnetised plasma flows with conducting obstacles

G. C. Burdiak, S. V. Lebedev, S. N. Bland, T. Clayson, J. Hare, L. Suttle, F. Suzuki-Vidal, D. C. Garcia, J. P. Chittenden, S. Bott-Suzuki, A. Ciardi, A. Frank, and T. S. Lane

The structure of bow shocks formed by the interaction of pulsed-power driven magnetised plasma flows with conducting obstacles

G. C. Burdiak,[1] S. V. Lebedev,[1] S. N. Bland,[1] T. Clayson,[1] J. Hare,[1] L. Suttle,[1] F. Suzuki-Vidal,[1] D. C. Garcia,[1] J. P. Chittenden,[1] S. Bott-Suzuki,[2] A. Ciardi,[3] A. Frank,[4] and T. S. Lane[5]

[1]*Blackett Laboratory, Imperial College London, London SW7 2BW, United Kingdom*
[2]*University of California San Diego, 9500 Gilman Drive, La Jolla, California 92093, USA*
[3]*Sorbonne Universités, UPMC University Paris 6, UMR 8112, LERMA, F-75005 Paris, France and LERMA, Observatoire de Paris, PSL Research University, CNRS, UMR 8112, F-75014 Paris, France*
[4]*Department of Physics and Astronomy, University of Rochester, Rochester, New York 14627, USA*
[5]*West Virginia University, Morgantown, West Virginia 26506, USA*

We present an experimental study of the development and structure of bow shocks produced by the interaction of a magnetised, collisional, super-Alfvénic plasma flow with conducting cylindrical obstacles. The plasma flow with an embedded, frozen-in magnetic field ($Re_M \sim 20$) is produced by the current-driven ablation of fine aluminium wires in an inverse, exploding wire array z-pinch. We show that the orientation of the embedded field with respect to the obstacles has a dramatic effect on the bow shock structure. When the field is aligned with the obstacle, a sharp bow shock is formed with a global structure that is determined simply by the fast magneto-sonic Mach number. When the field is orthogonal to the obstacle, magnetic draping occurs. This leads to the growth of a magnetic precursor and the subsequent development of a magnetised bow shock that is mediated by two-fluid effects, with an opening angle and a stand-off distance, that are both many times larger than in the parallel geometry. By changing the field orientation, we change the fluid regime and physical mechanisms that are responsible for the development of the bow shocks. MHD simulations show good agreement with the structure of well-developed bow shocks. However, collisionless, two-fluid effects will need to be included within models to accurately reproduce the development of the shock with an orthogonal B-field. *Published by AIP Publishing.*
[http://dx.doi.org/10.1063/1.4993187]

I. INTRODUCTION

Magnetic fields embedded in high Mach number plasma flows or intrinsic to obstructions play a vital role in determining the detailed structure of shocks formed at interfaces. In astrophysics, the effect of field morphology on supersonic flows can lead to important changes in the dynamics of environments that are as varied as star forming clouds, supernova remnants, and star–planet interactions.[1–4] Magnetic draping occurs when bodies propagating super-Alfvénically sweep up the magnetic field in an ambient medium, causing field lines to pile up and bend around the obstruction.[5] The draping process can lead to the buildup of a large scale, dynamically significant field and the development of magnetised bow shocks. Bow shocks can also form in collisionless magnetised flows such as the solar wind, and in these cases, the shock formation will be mediated by two-fluid effects (see, e.g., Ref. 6 and references therein) such as charge separation and the generation of a cross-shock potential. Magnetised shocks are also important in many ICF experiments, either because the fusion target is rapidly compressed onto a pre-imposed[7,8] or self-generated (e.g., R-T driven[9,10]) field, or because of deleterious magnetised flows generated by laser–hohlraum interactions.[11–14]

Performing experiments to study the physics of magnetized high energy density (HED) plasma flows represents a new field within laboratory astrophysics. Several computational studies exist (e.g., Refs. 1–4, 15, and 16); however, there are very few sufficiently diagnosed experimental studies for benchmarking of simulations. Progress has been made in producing supersonic, magnetized, laser driven plasma flows,[17,18] but the formation of flows with an embedded magnetic field remains a difficult task. Pulsed-power driven experiments provide a natural platform for producing magnetized HED plasma flows, and several experiments have demonstrated the formation of shocks where the magnetic field is important for the shock structure.[19–21]

In this paper, we show how the orientation of the magnetic field embedded in a supersonic ($M_S \equiv v_{flow}/c_S = 5$), super-Alfvénic ($M_A \equiv v_{flow}/v_A = 2$), plasma flow dramatically affects the structure of bow shocks formed around conducting, cylindrical obstructions. When the upstream magnetic field lies parallel to the obstacle, sharp bow shocks are formed with a global structure determined by the fast magneto-sonic Mach number. When the field is oriented perpendicular to the obstacle, magnetic draping occurs. This leads to the growth of a magnetic precursor and the subsequent development of a magnetised bow shock that is mediated by two-fluid effects, with an opening angle and a stand-off distance that are both many times larger than in the parallel geometry. By changing the field orientation, we change the fluid regime and physical mechanisms that are

responsible for the development of the bow shocks. The dataset provides a simple and quantitative test for numerical simulations that attempt to model magnetized HEDP systems. The test is especially stringent because collisional and collisionless dynamics are shown to manifest themselves within the same experiment.

II. EXPERIMENTAL SETUP AND THE PRODUCTION OF A MAGNETISED, SUPERSONIC FLOW

The plasma flow in these experiments is produced by an exploding (inverse) wire array z-pinch[22] that is driven by the Magpie[23] pulsed-power device at Imperial College London (1.4 MA, 240 ns rise-time). The current pulse ablates material from a cylindrical array of $25 \times 30 \, \mu m$ diameter aluminium (Al) wires that surround a central cathode rod (Fig. 1). The diameter of the wire array is 20 mm. The $\vec{j} \times \vec{B}$ force provided by the driving current accelerates the ablated material radially outwards to $\sim 100 \, km \, s^{-1}$ in a narrow ($\sim 1 \, mm$) sheath close to the wire cores. Within the acceleration region, some fraction of the azimuthal magnetic field becomes frozen into the electron component of the ablating plasma ($\omega_e \tau_e \sim 1$) and is advected outwards with the flow (magnetic Reynolds number $Re_M > 20$ for $L = 10 \, mm$),

allowing for the study of magnetised plasma dynamics and interactions. [Note that the ions remain unmagnetised ($\omega_i \tau_i \sim 10^{-2}$).] The plasma flow is further characterised by a low polytropic index $\gamma = 1.1–1.2$ (Ref. 24) and an internal collisional mean free path (mfp) $\lesssim 10 \, \mu m$. Figure 1(a) shows the electrode geometry for a 3D, resistive MHD Gorgon simulation of an inverse z-pinch used in the present experiments, together with a density slice of the ablating plasma 120 ns into the current pulse. In experiments and simulations, the full circumference of the array is wired to stop the magnetic flux from leaking through the array diameter and coupling directly to obstacles positioned some distance away. There is particularly close wire spacing on one side of the wire array to help produce a uniform flow with negligible divergence, for subsequent interaction with an obstacle. The 11 wires closest to the obstacle are positioned with an angular wire separation of $11.25°$ (at an inter-wire separation of $\sim 0.5 \, mm$ for a 20 mm array diameter). The remaining 14 wires have an angular separation of $22.5°$. Interactions between the discrete ablation streams of each wire act to reduce the contrast of the azimuthal density modulations to the level of 10% at the position of the obstacle (10 mm from the array), as can be seen in the interferometry data in Fig. 3(d). This modulation is small enough to allow for the formation of a smooth bow shock.

Cylindrical obstacles are positioned 10 mm from the ablating wires and oriented parallel or perpendicular to the advected field lines as shown in Figs. 1(b) and 1(c), respectively, with all other load parameters held constant between experiments. We refer to the two setups in Fig. 1 as the $B_\parallel$ and $B_\perp$ arrangements, respectively. The obstacles are formed from $500 \, \mu m$ diameter brass rods that extend beyond the flow–obstacle interaction region to avoid end-effects. By using cylindrical as opposed to more astrophysically relevant spherical obstructions, the relative importance of magnetic field draping (pile-up and bending) and slipping at the obstacle can be assessed. The development and structure of shocks are diagnosed using laser interferometric and Schlieren imaging (2 frames, 355 and 532 nm, 50 mJ, 0.5 ns probe[25]) and emission imaging (5 ns exposure, 12-frame optical, and 4-frame XUV). The imaging diagnostic field of view is arranged in each case so that the cylindrical targets point into the plane of the images. Flow velocity and plasma temperature (T_i, ZT_e) are determined via measurement of the collective Thomson scattering (TS) ion feature.[25–27] The magnetic field is measured using localised inductive ("B-dot") probes consisting of pairs of oppositely wound single loop coils. The opposite polarity signals produced are digitised independently without in-line amplification or integration. Small electric field contributions ($\sim 10\%$ of the B-field signal) are removed by combining signal pairs numerically. Multiple targets are fielded on each experiment so that the interaction of multiple bow shocks may be studied. These results will be the subject of a separate publication.

The ability to embed a dynamically significant magnetic field within a high Re_M plasma as a natural consequence of the plasma acceleration process is an appealing characteristic of pulsed-power driven laboratory astrophysics experiments. Advection of the magnetic field by the flow is clearly
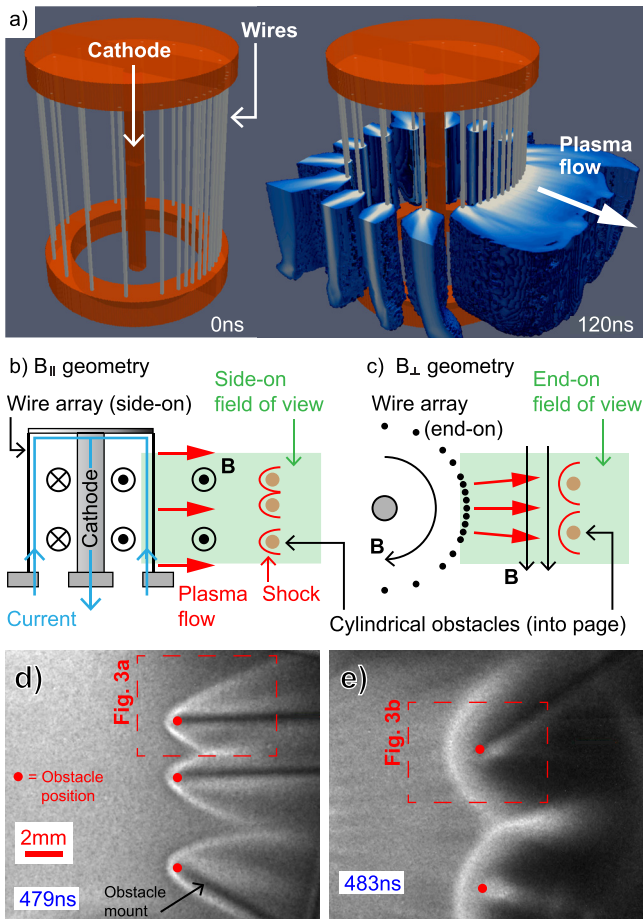
FIG. 1. Experimental setup. (a) Gorgon MHD simulation showing the inverse wire array configuration and a density slice through an ablating plasma at 120 ns. (b) and (c) Experimental geometries for an advected B-field parallel and perpendicular to obstacles. (d) and (e) Optical emission images of bow shocks in each geometry. Obstacle mounts seen as shadows in (d) and (e) are outside of the plasma flow.
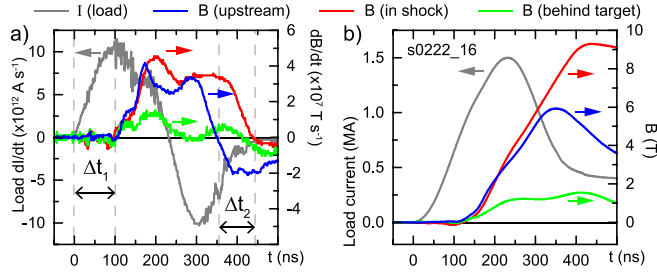
FIG. 2. (a) dB/dt waveforms at different positions (see Fig. 6 for guidance). The results were obtained during a $B_\perp$ experiment. The blue line shows the advected field in unobstructed flow, which is not affected by the obstacle orientation. The load dI/dt is shown for comparison. (b) Integrated waveforms showing the magnetic field and the load driving current.

demonstrated by measurements of dB/dt as shown in Fig. 2(a). The blue signal (labeled B upstream) was obtained using a B-dot probe positioned in a region of the flow unperturbed by the bow shock obstruction but at the same radial distance from the array. The B-dot signal has the same shape as the driving dB/dt ($\propto$ driving dI/dt, grey line), but it is shifted by the time-of-flight ($\Delta t_1 = 100$ ns) of plasma from the wire array to the probe. This is strong evidence that the B-field is frozen in and advected by the plasma flow, and that the magnetic field from the generator discharge does not couple directly to the obstacle structure.

III. THE STRUCTURE OF MAGNETISED BOW SHOCKS WITH DIFFERENT MAGNETIC FIELD ORIENTATIONS

The contrasting overall structure of bow shocks in each field geometry is shown in the optical emission images in Fig. 1. The plasma flow propagates from the left. Emission at the leading edge of the obstacles is observed from 100 ns into the current pulse, when plasma from the wire array first interacts. In the left-hand panel the embedded magnetic field is aligned parallel to three target cylinders and into the page. Stagnation of this plasma onto the obstacles together with ablation of the obstacles generates reverse shocks into the flow. These develop into sharp bow shocks which persist for several hundred nanoseconds in a stationary state whilst the wire array continues to ablate. In the right-hand panel, the magnetic field is aligned normal to two target cylinders and up-down in the plane of the image. In this geometry,
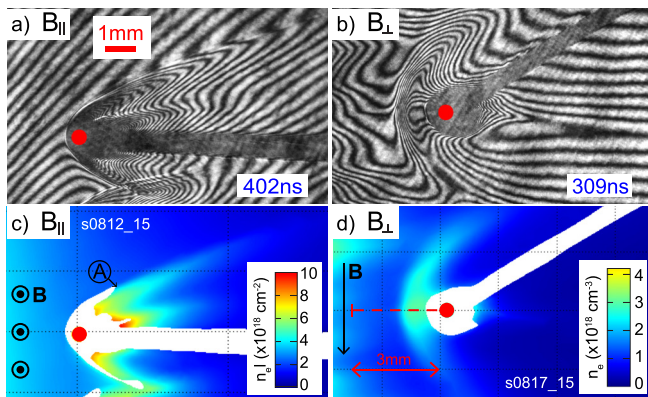

FIG. 3. Interferograms and electron density maps for regions outlined in Fig. 1. Red spots indicate target positions.

detached bow shocks are formed much further from the obstacle, and with a much larger opening angle. The $B_\perp$ shock is observed from 200 ns into the current pulse, and again remains stationary for ≥ 200 ns. The material in the downstream flow continues to interact with the target, creating an additional attached density structure, clearly seen in the interferometry data in Fig. 3.

Interferometry data are used to perform a more quantitative analysis of the different bow shock structures. Figures 3(a) and 3(b) show interferogram details of each system. Interferograms were analysed using the method described in Ref. 24 to produce line-integrated (areal) electron density ($n_e l$) maps [e.g., Fig. 3(c)]. In the $B_\perp$ arrangement [Fig. 3(d)], the plasma is nominally uniform along the line of sight (which is confirmed by side-on probing) and the depth of the interaction along the cylindrical targets is set by the wire array length, z_0. In this case, we can produce maps of n_e ($= n_e l/z_0$).

The geometry of the $B_\parallel$ shock is consistent with an MHD description of the flow. Interference fringes at the leading edge of the bow are lost because of very strong density gradients, indicative of a collisional shock. In the oblique limb of the shock (e.g., position "A," shock angle $\beta \sim 30°$), n_e increases by a factor of ~ 2.5. For a normal shock, e.g., at the leading edge of the bow, this would correspond to a density compression of $2.5/\sin(30°) = 5$. This does not contradict the density jump expected for $\gamma = 1.1$–$1.2 \ll 5/3$. The Mach number of the upstream flow can be calculated from the Mach angle, α, via $M = 1/\sin\alpha$. From the geometry observed in Schlieren, emission and interferometry images, $M = 2.4$–2.6. The values of M_S and M_A were also calculated from plasma parameters measured using TS, interferometry and B-dots. These are equal to $M_S = 5.0 \pm 0.5$ and $M_A = 2.2 \pm 0.3$, and are roughly constant in time. The individual plasma parameters are, however, time-dependent. As a reference, typical flow parameters at the times of the diagnostic images (300–400 ns) are $v_{flow} = 60$–75 km s^{-1}, $B = 5$–6 T, $n_e = 1$–3×10^{18} cm^{-3}, $T_i = 10$–15 eV, and $ZT_e = 40$–50 eV. The fast magneto-sonic Mach number is given by the following expression: $M_{MS} = M_S.M_A/\left(M_S^2 + M_A^2\right)^{1/2}$. Using the measured values of M_S and M_A, M_{MS} is determined to be equal to 1.8–2.2. This range of M_{MS} is close to M calculated using the shock geometry and is dominated by M_A. Throughout the remainder of the paper, we take the effective Mach number of the flow to range from $M = 2$–2.5. Overall, in the $B_\parallel$ geometry, the B-field affects the plasma compressibility. However, due to the small obstacle diameter, the flow and B-field are able to slip past, which limits the pile-up of the B-field ahead of the obstacle.

In contrast, the draping of the magnetic field in the $B_\perp$ geometry causes a larger B-field pile-up and the appearance of a magnetic tension force contribution, leading to the development of a shock with a very different structure. Measurements of the temporal evolution of the $n_e(x)$ profile across the shock, shown in Fig. 4, demonstrate that it develops as the gradual steepening of a density enhancement, which is first detected at $t \approx 200$ ns, 1.5 mm from the obstacle. This initially small density perturbation grows whilst the spatial position remains constant for ≥ 200 ns. The slowing down mfp, $\lambda_s^{i\backslash i}$,[28] of the directed ion flow on the enhanced
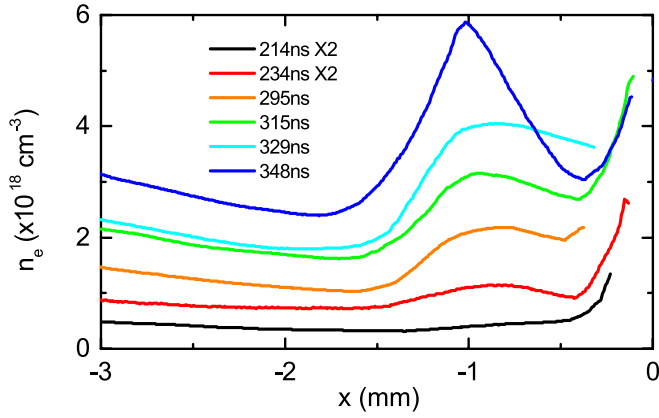
FIG. 4. Time series of n_e profiles along the red dashed line in (d). 214 and 234 ns profiles are multiplied by 2 for ease of presentation. Data obtained from interferograms are similar to those presented in Fig. 3.

ion density is time-dependent and decreases rapidly during experiments due to the increasing flow density and the gradual reduction of the flow velocity of the wire array ablation streams.[29,30] At the time of shock formation (210 ns), $\lambda_s^{i \backslash i} \approx 2.5$ mm, whereas by 350 ns, $\lambda_s^{i \backslash i}$ has reduced to 30 μm. The large stand-off shock forms whilst the streaming ion flow is quite collisionless. It is very interesting to note that qualitatively the density profile of the shock then persists throughout and beyond the transition to a collisional regime. This structure cannot be explained by a change in the properties of the upstream flow, which remain identical to the $B_\parallel$ experiments. We interpret these observations as being a result of the draping of the magnetic field over the obstacle and the generation of currents along the length of the obstacle and shock. We stress that a collisional MHD shock, as in the $B_\parallel$ case, would necessarily form at the obstacle surface, and only then propagate upstream.

A. Detailed structure of the $B_\perp$ shock

The pile-up of magnetic flux at the obstacle in the $B_\perp$ geometry is evident in the measurements of $B(t)$ made within the shock and behind the obstacle [Fig. 2, representative positions indicated in Fig. 6(a)]. The magnetic field within the shock continues to rise for $\Delta t_2 = 90$ ns longer than the field within the unperturbed flow. The field is compressed as the falling edge of the advected temporal profile continues to pile up onto the field accumulated ahead of the obstacle. Simultaneously, the field behind the obstacle is depleted. These observations indicate that an induced current is generated along the length of the obstacle. The induced current must return via a closed loop formed by the shock and the edges of the plasma, in a manner similar to that discussed in Refs. 21 and 31. This situation is depicted in the "side-on" images in Fig. 5 and is discussed further in Sec. III C.

The ram pressure of the super-Alfvénic upstream flow results in bending of the piled up field lines, which determines the shape of the bow. The magnetic draping effect results in a redirection of the flow as transport along the curved field lines is relatively uninhibited, and this could affect the level of density increase at the shock. TS measurements were performed to investigate the flow structure. The

geometry of the TS setup is shown in Fig. 6(a). The TS probe (532 nm, 5 ns FWHM, 2 J, $\varnothing \sim 200$ μm) enters the load region parallel to either the x or y axis. Scattered light from discrete volumes along the length of the probe is imaged onto a fibre optic array positioned at 90° to the input probe k-vector, k_{in}, in the manner described in Refs. 21 and 32. This setup enables localised measurements of the bulk plasma velocity component along the probing direction. Figure 6(a) shows the TS collection volumes superimposed onto a simultaneous, measured n_e distribution. Figure 6(b) shows the raw TS spectra for each TS probing beam orientation. The TS spectra were fit [e.g., Fig. 6(c)] to determine T_i, ZT_e and the plasma velocity. The measurements of ZT_e, T_i and plasma velocity were then used to calculate c_S and M_S. The measurements of ZT_e and n_e (n_e from interferometry) were also used together with nLTE atomic physics calculations performed using Spk[33] to determine self-consistent values of Z and T_e. Note that an independent determination of Z via TS in our regime is only theoretically possible if the TS system is absolutely calibrated.

Velocity measurements along $\hat{x}$ and $\hat{y}$ at the positions indicated in Fig. 6(a) are plotted in Figs. 6(d) and 6(e) together with the n_e profile along $k_{in}(\hat{x})$. The low plasma density and the increased stray light in the downstream region prevent the accurate measurement of v_x from the final 4 red collection volumes shown in Fig. 6(a). The measurements show an average upstream flow velocity of $v_x = 77$ km s^{-1}. This velocity component gradually decreases by a modest factor of $\sim$2, as the flow passes through the shock. It is a very interesting and surprising result that the velocity begins to decrease *before* n_e begins to increase. The causes for this will be explored in future work. The symmetric deflection of the upstream flow around the obstacle is clearly demonstrated in the measurement of lateral velocity (v_y) along $k_{in}(\hat{y})$ shown in Fig. 6(e). The lateral velocity outside of the shock is close to zero. Within the shock, v_y reaches a maximum of ± 17 km s^{-1}, but remains close to zero
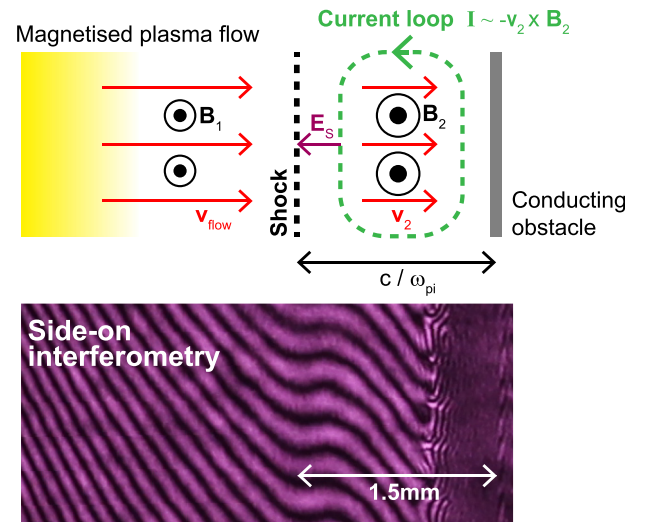

FIG. 5. (a) Side-on schematic of a current loop formed by the compression of an advected flux against a conducting obstacle. (b) Side-on interferogram showing the shock along a short segment of the obstacle length. The interferogram is aligned and to scale with the schematic above.
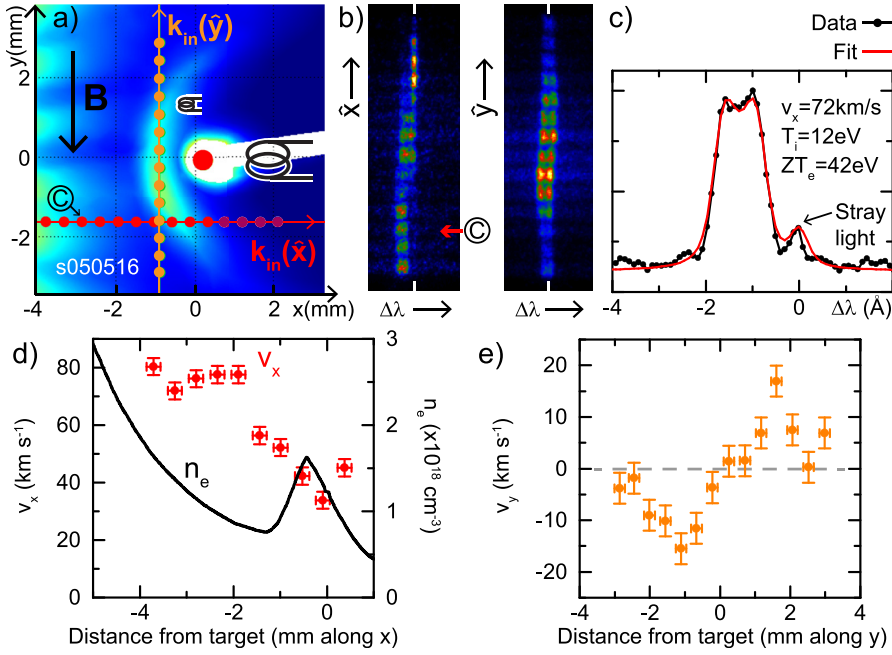
FIG. 6. (a) TS input vectors and collection volumes (small spots) on a n_e map. $B_\perp$ configuration. Coils show the locations of B-dot pairs fielded on a separate experiment in relation to data in Fig. 2. (b) Raw TS spectra obtained for $k_{in}(\hat{x})$ and $k_{in}(\hat{y})$. (c) TS spectrum (black) and fit (red) obtained in the upstream flow along $\hat{x}$. (d) and (e) Plots of v_x and v_y along the two input k vectors.

immediately in front of the obstacle. Overall, the velocity measurements demonstrate that the flow is decelerated and deflected around the obstacle. The large stand-off of the redirection region is consistent with deflection by field lines that are draped (piled up and curved) over the obstacle. TS spectral fits show a small increase in T_i from 10 ± 2 eV in the upstream flow to 15 ± 3 eV in the shock. This increase is a factor of 3–4 too small to account for the loss of directed kinetic energy at the shock, even when assuming equipartition of energy with the electrons. This suggests that the ions are not undergoing strong collisional heating at the shock front. The gradual reduction of the ion flow velocity seen in Fig. 6(d) could be caused by a decelerating cross shock potential, with a limited increase of the ion temperature.

The density jump at the $B_\perp$ shock is much smaller than for the $B_\parallel$ case. Interferometry data in Fig. 4 show that n_e increases by a factor of only 2–2.5. From the TS measurements of ZT_e combined with an nLTE ionisation model, the average ionisation increases from 3.5 to 4. These numbers give a mass density ratio across the shock of $\Gamma = 1.75$–2.2. This ratio is consistent with the observed decrease in the flow velocity by a factor of ∼2, given the condition for momentum conservation ($\rho_0 u_0 = \rho_1 u_1$) across the shock boundary. The low compressibility of the downstream plasma can be quantified by calculating the effective polytropic index, γ_{eff}, using the following standard expression:

$$\gamma_{eff} = \frac{(M^2/\Gamma) + M^2 - 2}{M^2 - (M^2/\Gamma)}. \tag{1}$$

The above expression is plotted as a function of Mach number for various compression ratios in Fig. 7. The realistic parameter range of interest is shaded in orange and shows that γ_{eff} lies in the range 1.8–2.9, far from the hydrodynamic $\gamma = 1.1$–1.2 of ablation streams from Al plasmas reported previously,[24] which works to explain the geometry of $B_\parallel$ shocks. Taking median values for $M(= 2.25)$ and $\Gamma(= 2)$

yields $\gamma_{eff} = 2.3$. This estimate for γ_{eff} suggests that compressibility is strongly reduced in the $B_\perp$ setup, as may be expected given the low thermal plasma beta (0.1–0.5) both upstream and downstream of the shock. The large value of γ_{eff} is consistent with the behaviour of strongly magnetised transverse (B_y) shocks, where only 2 degrees of freedom (v_x, v_z) are involved and $\gamma = 1 + (2/n_d) = 2$.

B. The importance of the obstacle diameter and resistivity

The pile-up of the advected magnetic flux only occurs in the $B_\perp$ geometry if the obstacle conductivity is sufficient to prevent flux diffusion. The large stand-off magnetic shock does not form when the brass target is replaced with an insulating glass rod of the same dimensions. Figure 8 shows two bow shocks produced side-by-side within the same experiment, around one conducting and one insulating obstacle. The shape of the bow differs drastically between the two cases. For the insulating glass obstacle, the shape of the bow returns to the shape observed in the $B_\parallel$ geometry, indicating
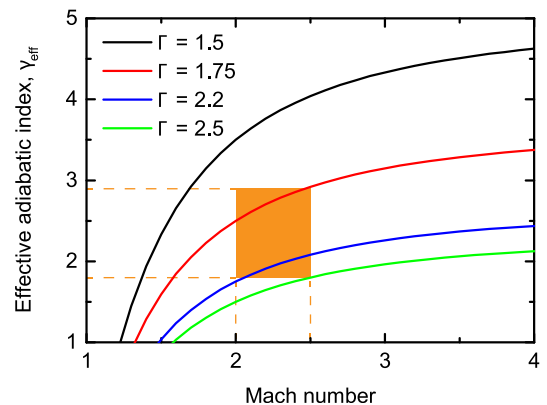

FIG. 7. Plots of the effective polytropic index versus the Mach number for various compression ratios, calculated using Eq. (1). The shaded area denotes the error bounds of the experimental data.
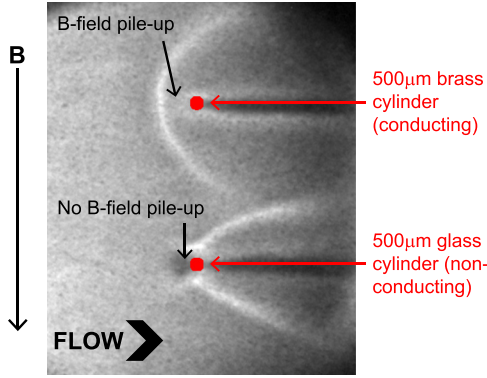
FIG. 8. Optical emission images showing contrasting bow shocks formed around conducting and insulating obstacles in the $B_\perp$ geometry. Shocks are formed side-by-side in the same experiment. The leading edge of the shock around the glass target is blocked by the target mount.

that magnetic draping does not occur. From the Mach angle, in this case, we find $M_{MS} = 2.1$–2.4, again consistent with the measured upstream parameters. This confirms that the induced current supporting the large stand-off shock is driven through the obstacle, not the stagnated plasma layer surrounding it.

The efficacy of the flux pile-up also depends on the obstacle diameter. It was found that the large stand-off bow shock did not form for a 50 μm conducting copper target. This result is probably caused by the finite skin depth, or diffusion length, of the transient magnetic pulse arriving at the obstacle. The magnetic skin depth is given by $\delta_s = (2/\mu_0 \sigma \omega)^{1/2}$, where ω is the frequency of the current pulse and σ is the obstacle conductivity. Over distances of this order, the magnetic flux will diffuse into a non-perfect conductor. If the obstacle resistivity and dimensions are such that the obstacle cannot support sufficient induced current, then the perpendicular magnetic field lines can pass through unimpeded. In Fig. 9, the shock stand-off distance observed in several different experiments has been plotted against the ratio of the conductor skin depth to the diameter, D, of the cylindrical target. We assume that the characteristic frequency for the advected magnetic field at the target is equal to the driving current frequency ($\omega = 2\pi/ 480$ ns). It is found that below a ratio of $\delta_s/D \sim 2$, the standoff begins to decrease from 1.5 mm. The large stand-off shock
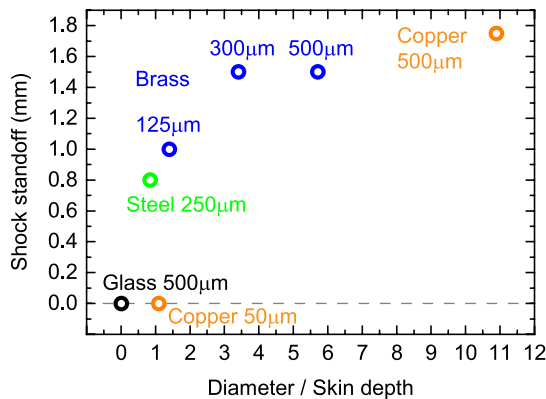

FIG. 9. Shock stand-off distance as a function of obstacle diameter/magnetic skin depth. The stand-off decreases if the obstacle conductivity or diameter is small.

does not form if either the resistivity is very high (500 μm glass) or the diameter is very small (50 μm Cu).

C. A model for the development of the $B_\perp$ bow shock

As discussed in Sec. III, the $B_\perp$ shock develops at a large stand-off distance as the gradual steepening of a density enhancement, which is mediated by a buildup of magnetic pressure ahead of the obstacle. The fixed 1.5 mm stand-off distance throughout the shock development was a surprising result. Here, we present a model to explain these observations.

The size of the region ahead of the obstacle with an increased magnetic field is determined by the balance of magnetic field advection by the flow and the diffusion of the draped, compressed field into the upstream plasma. In a simple model, the rate of diffusion sets the width of the magnetic precursor, $\delta_m(t)$,

$$\delta_m(t) = \sqrt{(2D_M t)}, \tag{2}$$

where D_M is the magnetic diffusivity. From TS measurements of T_e we find $D_M \sim 10^5$ cm^2 s. The average strength of the magnetic field in the precursor is given by the following expression:

$$B_{pr} = \frac{\int B_{in}(t) v_f(t) dt}{\delta_m(t)}, \tag{3}$$

where B_{in} and v_f are the measured time-dependent advected magnetic field and the upstream flow velocity, respectively. The temporal velocity profile was fitted to time-of-flight and TS data accumulated over several experiments. These measured parameters are plotted together with B_{pr} in Fig. 10(a). The significance of the accumulated magnetic field is determined by the dynamic beta parameter, β_{dyn}, which is the ratio of the flow ram pressure to the accumulated magnetic pressure. The final equality in Eq. (4) allows β_{dyn} to be calculated using our previous determination of M_A, which we found to be approximately constant over several hundred ns,

$$\beta_{dyn} = \frac{\rho v_f^2}{B_{pr}^2/2\mu_0} = \frac{B_{in}^2}{\mu_0 v_A^2} \cdot \frac{v_f^2}{B_{pr}^2/2\mu_0} = \frac{B_{in}^2}{B_{pr}^2} \cdot 2M_A^2. \tag{4}$$

Plots of $\beta_{dyn}(t)$, $\delta_m(t)$ and ion inertial length, $c/\omega_{pi}(t)$, are presented in Fig. 10(b). At early times, $\beta_{dyn} \gg 1$, and the accumulated magnetic field has little effect on the incoming flow. However, as time progresses, β_{dyn} approaches unity and the magnetic field will begin to decelerate the magnetised electrons. At 200 ns, corresponding to the time of formation of the shock, we find that $\beta_{dyn} \sim 1$. Simultaneously, we find that our estimate for the diffusion length, or precursor width, δ_m, is equal to 1.5 mm, corresponding to the observed stand-off distance of the shock. These observations strongly suggest that the shock forms at the foot of a magnetic precursor. The development of the shock must be driven by the preferential deceleration of the electrons, because the relatively heavy ions remain unmagnetised. Therefore an additional mechanism is required to explain the deceleration of the ions observed by TS measurements. As shown in Fig. 10(b), at the time of shock formation, the ion-inertial length, c/ω_{pi}, is also close to
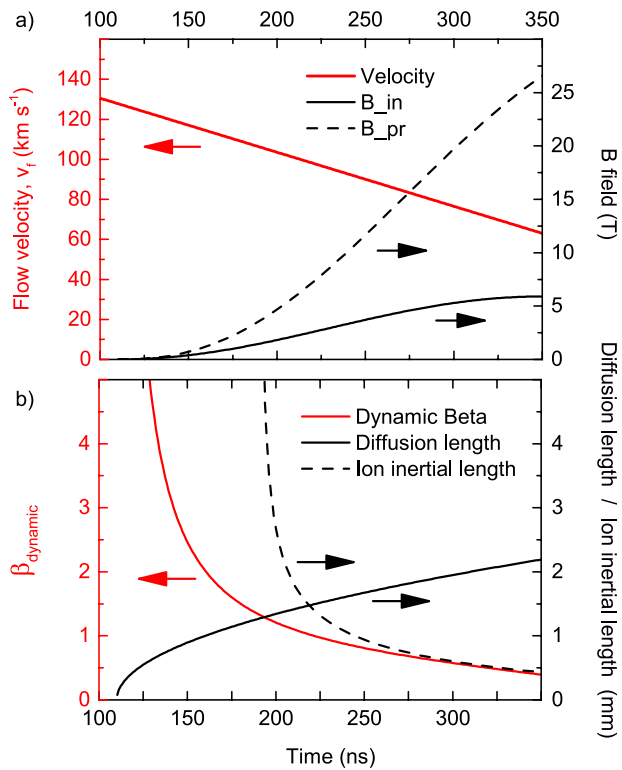
FIG. 10. Model for the development of a magnetised shock at a large stand-off distance from the obstacle. (a) Upstream flow velocity, advected magnetic field and accumulated magnetic field ahead of the target. (b) The shock forms at 200 ns, when the dynamic beta = 1, at a distance equal to the magnetic diffusion length and the ion inertial length.

the shock stand-off distance (1.5 mm). As a result, the ion and electron responses to the enhanced field are able to decouple over the spatial scale length of the magnetic precursor. This decoupling could generate a cross-shock E field, causing a subsequent deceleration of the unmagnetised ions. The diffusion model and the 2-fluid deceleration mechanism are consistent with the experimental data, and together can explain the surprising observation of the development of a compressed region far from the obstacle.

IV. MHD SIMULATION RESULTS AND CONCLUSIONS

In summary, this work demonstrates that the orientation of an embedded magnetic field within a super-Alfvénic HED plasma flow is vital to determining the development mechanism and the subsequent structure of bow shocks formed around conducting, cylindrical obstructions. When the magnetic field and obstacles are aligned, the bow shock in the experiments is formed by a collisional process. The magnetic field affects the opening angle of the bow shock by reducing the (magnetosonic) Mach number. However, the magnetic field has a negligible effect on the plasma compressibility at the shock front itself because the shock width, which is determined by the collisional scale length, is smaller than the magnetic diffusion scale length. In contrast, when the upstream magnetic field lies perpendicular to the obstacle, magnetic draping results in the development of a region of enhanced magnetic field in the upstream plasma, produced by the pile-up of the advected field. This

leads to the formation of a large stand-off bow shock via the preferential slowing of magnetised electrons, and a subsequent deceleration of ions by the generation of a cross-shock potential. The bow shock in this geometry has a large opening angle resulting from tension in the draped magnetic field lines.

Resistive MHD codes are often employed to simulate HEDP experiments. The clean geometry, well-defined initial conditions and thorough diagnosis of these experiments make them suitable for benchmarking numerical simulations in a magnetised regime. 3D simulations of these experiments were performed using the Gorgon MHD code.[34] These simulations modeled the full, current-driven explosion of the inverse wire array z-pinch [see Fig. 1(a)] to produce a time-dependent plasma flow that impacted conducting cylinders. The results of the simulations are shown in Fig. 11.

The simulations compare favourably to the experimental data at later times, when the bow shocks are fully developed and collisional MHD dominates the flow interactions. The bow shock in the $B_\parallel$ setup has a sharp shock front, a small obstacle stand-off and a narrow opening angle, whereas the bow shock in the $B_\perp$ setup has a more gradual shock transition, a large stand-off and a wide opening angle.

The development of the $B_\parallel$ shock is also accurately reproduced by the simulations. This is because the shock is mediated by the collisional stagnation of the plasma flow at the obstacle surface. The development phase of the $B_\perp$ shock is not fully reproduced by the simulations. Instead of forming at a large stand-off distance ($\sim$1.5 mm) as observed in experiments, the shock forms at the obstacle surface and then propagates outwards as time progresses. This observation supports our argument that the shock development is mediated by two-fluid effects, which are not included in the numerical model. As discussed in Sec. III, the shock in experiments forms at a
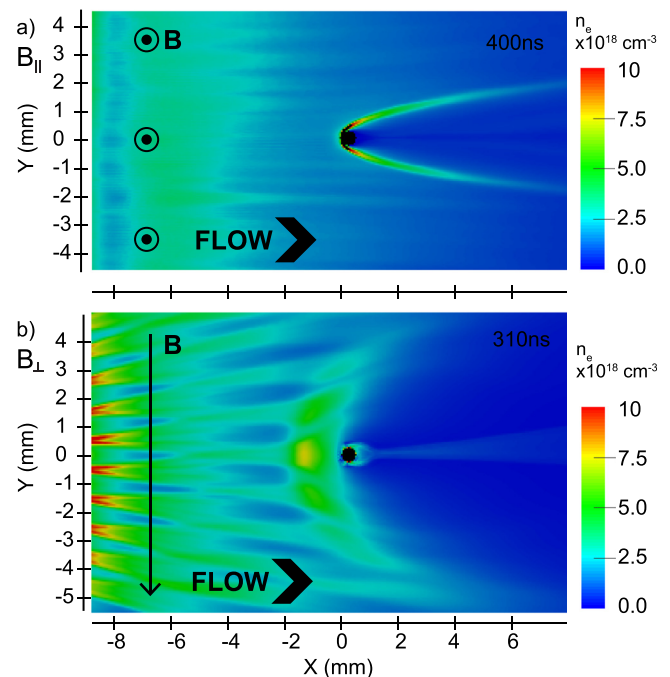

FIG. 11. 2D electron density slices from 3D Gorgon MHD simulations of $B_\parallel$ (upper panel) and $B_\perp$ (lower panel) experiments.

time when the streaming ion flow is quite collisionless ($\lambda_s^{i \backslash i} \approx 2.5$ mm), and therefore we would not expect an MHD model to fully capture the formation dynamics.

The simulations show perturbations in the upstream flow that are due to both the axial modulation of the wire ablation rate [Fig. 11(a); see, e.g., Ref. 22) and the discrete nature of the ablating wires [Fig. 11(b)]. In Fig. 11(b), the perturbations are sufficient to imprint upon the global bow shock structure. Whilst both of these phenomena are observable in wire array experiments, in the present work we are able to produce a plasma flow with a much smaller degree of modulation than is suggested by the simulations (see Figs. 1 and 3), and as a result, smooth bow shocks are formed in both geometries. The discrepancies discussed here are currently under investigation.

Further modelling was performed using the "extended" MHD (XMHD) code Perseus, which includes the Hall term within the equation for Ohm's Law, whilst still imposing quasi-neutrality. This term describes the *Hall* effect, which allows for a B-field advection velocity that is different from the bulk velocity. It can be important on spatial scales within the ion inertial length, c/ω_{pi} (see, e.g., Ref. 35). Perseus has been used previously to study the interaction of magnetised flows with obstacles.[16] Simulation results within[16] showed that the Hall term was important for the magnetotail structure behind the obstacles, but that it had no impact on the bow shock stand-off distance. Simulations of the present experiments using Perseus show qualitative agreement with the global structure of well-developed bow shocks. However, the formation phase of the $B_\perp$ shock again remains to be fully reproduced. These observations further strengthen our argument that the development of the $B_\perp$ shock is driven by 2-fluid effects, which cannot be described even by Hall-MHD.

Computational work with these two MHD codes is ongoing. However, accurate modelling of the $B_\perp$ shock formation will probably require non-local effects to be included, such as the separation of electron and ion bulk velocities occurring on the c/ω_{pi} spatial scale and sophisticated particle collision models. Fully kinetic 3D particle-in-cell (PIC) modelling could present a useful way forward. These methods have been employed previously to study magnetospheres,[6] which exhibit many similarities with the present work, including bow shock stand-off distances on the order of c/ω_{pi}. The data presented here could provide a simple test problem for PIC models.

ACKNOWLEDGMENTS

[1]S. Li, A. Frank, and E. G. Blackman, Astrophys. J. **774**, 133 (2013); e-print arXiv:1307.3316 [astro-ph.SR].

[2]S. Orlando, F. Bocchino, F. Reale, G. Peres, and P. Pagano, Astrophys. J. **678**, 274–286 (2008); e-print arXiv:0801.1403.

[3]G. Gregori, F. Miniati, D. Ryu, and T. W. Jones, Astrophys. J. **543**, 775 (2000).

[4]M. Titos, U. Ana, and K. Arieh, Astron. Astrophys. **578**, A6 (2015).

[5]L. J. Dursi and C. Pfrommer, Astrophys. J. **677**, 993 (2008).

[6]R. A. Bamford, E. P. Alves, F. Cruz, B. J. Kellett, R. A. Fonseca, L. O. Silva, R. M. G. M. Trines, J. S. Halekas, G. Kramer, E. Harnett, R. A. Cairns, and R. Bingham, Astrophys. J. **830**, 146 (2016).

[7]S. A. Slutz, M. C. Herrmann, R. A. Vesey, A. B. Sefkow, D. B. Sinars, D. C. Rovang, K. J. Peterson, and M. E. Cuneo, Phys. Plasmas **17**, 056303 (2010).

[8]P. Y. Chang, G. Fiksel, M. Hohenberger, J. P. Knauer, R. Betti, F. J. Marshall, D. D. Meyerhofer, F. H. Séguin, and R. D. Petrasso, Phys. Rev. Lett. **107**, 035006 (2011).

[9]R. G. Evans, Laser Part. Beams **4**, 325 (1986).

[10]L. Gao, P. M. Nilson, I. V. Igumenschev, S. X. Hu, J. R. Davies, C. Stoeckl, M. G. Haines, D. H. Froula, R. Betti, and D. D. Meyerhofer, Phys. Rev. Lett. **109**, 115001 (2012).

[11]R. S. Craxton and M. G. Haines, Phys. Rev. Lett. **35**, 1336 (1975).

[12]A. S. Joglekar, A. G. R. Thomas, W. Fox, and A. Bhattacharjee, Phys. Rev. Lett. **112**, 105004 (2014).

[13]C. K. Li, F. H. Séguin, J. A. Frenje, R. D. Petrasso, P. A. Amendt, R. P. J. Town, O. L. Landen, J. R. Rygg, R. Betti, J. P. Knauer, D. D. Meyerhofer, J. M. Soures, C. A. Back, J. D. Kilkenny, and A. Nikroo, Phys. Rev. Lett. **102**, 205001 (2009).

[14]A. S. Joglekar, C. P. Ridgers, R. J. Kingham, and A. G. R. Thomas, Phys. Rev. E **93**, 043206 (2016).

[15]A. S. Liao, S. Li, P. Hartigan, P. Graham, G. Fiksel, A. Frank, J. Foster, and C. Kuranz, High Energy Density Phys. **17**(Part A), 38 (2015).

[16]X. Zhao and C. E. Seyler, Phys. Plasmas **22**, 072102 (2015).

[17]M.-E. Manuel, C. Kuranz, A. Rasmus, S. Klein, M. MacDonald, M. Trantham, J. Fein, P. Belancourt, R. Young, P. Keiter, R. Drake, B. Pollock, J. Park, A. Hazi, G. Williams, and H. Chen, High Energy Density Phys. **17**(Part A), 52 (2015).

[18]B. Albertazzi, A. Ciardi, M. Nakatsutsumi, T. Vinci, J. Béard, R. Bonito, J. Billette, M. Borghesi, Z. Burkley, S. N. Chen, T. E. Cowan, T. Herrmannsdörfer, D. P. Higginson, F. Kroll, S. A. Pikuz, K. Naughton, L. Romagnani, C. Riconda, G. Revet, R. Riquier, H.-P. Schlenvoigt, I. Y. Skobelev, A. Faenov, A. Soloviev, M. Huarte-Espinosa, A. Frank, O. Portugall, H. Pépin, and J. Fuchs, Science **346**, 325 (2014).

[19]D. J. Ampleford, C. A. Jennings, G. N. Hall, S. V. Lebedev, S. N. Bland, S. C. Bott, F. Suzuki-Vidal, J. B. A. Palmer, J. P. Chittenden, M. E. Cuneo, A. Frank, E. G. Blackman, and A. Ciardi, Phys. Plasmas **17**, 056315 (2010).

[20]S. C. Bott-Suzuki, L. S. Caballero Bendixsen, S. W. Cordaro, I. C. Blesener, C. L. Hoyt, A. D. Cahill, B. R. Kusse, D. A. Hammer, P. A. Gourdain, C. E. Seyler, J. B. Greenly, J. P. Chittenden, N. Niasse, S. V. Lebedev, and D. J. Ampleford, Phys. Plasmas **22**, 052710 (2015).

[21]S. Lebedev, L. Suttle, G. Swadling, M. Bennett, S. Bland, G. Burdiak, D. Burgess, J. Chittenden, A. Ciardi, A. Clemens, G. P. de, G. Hall, J. Hare, N. Kalmoni, N. Niasse, S. Patankar, L. Sheng, R. Smith, F. Suzuki-Vidal, J. Yuan, A. Frank, E. Blackman, and R. Drake, Phys. Plasmas **21**, 056305 (2014).

[22]A. J. Harvey-Thompson, S. V. Lebedev, S. N. Bland, J. P. Chittenden, G. N. Hall, A. Marocchino, F. Suzuki-Vidal, S. C. Bott, J. B. A. Palmer, and C. Ning, Phys. Plasmas **16**, 022701 (2009).

[23]I. H. Mitchell, J. M. Bayley, J. P. Chittenden, J. F. Worley, A. E. Dangor, M. G. Haines, and P. Choi, Rev. Sci. Instrum. **67**, 1533 (1996).

[24]G. F. Swadling, S. V. Lebedev, N. Niasse, J. P. Chittenden, G. N. Hall, F. Suzuki-Vidal, G. Burdiak, A. J. Harvey-Thompson, S. N. Bland, P. De Grouchy, E. Khoory, L. Pickworth, J. Skidmore, and L. Suttle, Phys. Plasmas **20**, 022705 (2013).

[25]G. F. Swadling, S. V. Lebedev, G. N. Hall, S. Patankar, N. H. Stewart, R. A. Smith, A. J. Harvey-Thompson, G. C. Burdiak, P. de Grouchy, J. Skidmore, L. Suttle, F. Suzuki-Vidal, S. N. Bland, K. H. Kwek, L. Pickworth, M. Bennett, J. D. Hare, W. Rozmus, and J. Yuan, Rev. Sci. Instrum. **85**, 11E502 (2014).

[26]D. H. Froula, S. H. Glenzer, N. C. Luhmann, and J. Sheffield, *Plasma Scattering of Electromagnetic Radiaion* (Elsevier, 2011).

[27]A. J. Harvey-Thompson, S. V. Lebedev, S. Patankar, S. N. Bland, G. Burdiak, J. P. Chittenden, A. Colaitis, P. De Grouchy, G. N. Hall, E. Khoory, M. Hohenberger, L. Pickworth, F. Suzuki-Vidal, R. A. Smith, J. Skidmore, L. Suttle, and G. F. Swadling, Phys. Plasmas **19**, 056303 (2012).

[28]B. A. Trubnikov, Rev. Plasma Phys. **1**, 105 (1965).

[29]S. V. Lebedev, F. N. Beg, S. N. Bland, J. P. Chittenden, A. E. Dangor, M. G. Haines, K. H. Kwek, S. A. Pikuz, and T. A. Shelkovenko, Phys. Plasmas **8**, 3734 (2001).

[30]G. F. Swadling, S. V. Lebedev, A. J. Harvey-Thompson, W. Rozmus, G. Burdiak, L. Suttle, S. Patankar, R. A. Smith, M. Bennett, G. N. Hall, F. Suzuki-Vidal, S. Bland, and J. Yuan, Phys. Plasmas **22**, 072706 (2015).

[31]G. Haerendel, L. Suttle, S. V. Lebedev, G. F. Swadling, J. D. Hare, G. C. Burdiak, S. N. Bland, J. P. Chittenden, N. Kalmoni, A. Frank, R. A. Smith, and F. Suzuki-Vidal, Plasma Phys. Controlled Fusion **58**, 064001 (2016).

[32]A. J. Harvey-Thompson, S. V. Lebedev, S. Patankar, S. N. Bland, G. Burdiak, J. P. Chittenden, A. Colaitis, P. De Grouchy, H. W. Doyle, G. N. Hall, E. Khoory, M. Hohenberger, L. Pickworth, F. Suzuki-Vidal, R. A. Smith, J. Skidmore, L. Suttle, and G. F. Swadling, Phys. Rev. Lett. **108**, 145002 (2012).

[33]J. P. Chittenden, B. D. Appelbe, F. Manke, K. McGlinchey, and N. P. L. Niasse, Phys. Plasmas **23**, 052708 (2016).

[34]A. Ciardi, S. V. Lebedev, A. Frank, E. G. Blackman, J. P. Chittenden, C. J. Jennings, D. J. Ampleford, S. N. Bland, S. C. Bott, J. Rapley, G. N. Hall, F. A. Suzuki-Vidal, A. Marocchino, T. Lery, and C. Stehle, Phys. Plasmas **14**, 056501 (2007).

[35]D. D. Ryutov, IEEE Trans. Plasma Sci. **43**, 2363 (2015).